The Effect of Nanoparticle Polyethylene Glycol Surface Density on Ligand-Directed Tumor Targeting Studied *in Vivo* by Dual Modality Imaging

Sjoerd Hak,[†,*] Emily Helgesen,[‡] Helga H. Hektoen,[‡] Else Marie Huuse,[†] Peter A. Jarzyna,[§] Willem J.M. Mulder,[§] Olav Haraldseth,[†,§] and Catharina de Lange Davies[‡]

[†]MI Lab and Department of Circulation and Medical Imaging and [‡]Department of Physics, The Norwegian University of Science and Technology, Trondheim, Norway, [§]Translational and Molecular Imaging Institute, Mount Sinai School of Medicine, New York, New York, United States, and [§]Department of Medical Imaging, St. Olav's University Hospital, Trondheim, Norway

ABSTRACT The development and application of nanoparticles as *in vivo* delivery vehicles for therapeutic and/or diagnostic agents has seen a drastic growth over the last decades. Novel imaging techniques allow real-time *in vivo* study of nanoparticle accumulation kinetics at the level of the cell and targeted tissue. Successful intravenous application of such nanocarriers requires a hydrophilic particle surface coating, of which polyethylene glycol (PEG) has become the most widely studied and applied. In the current study, the effect of nanoparticle PEG surface density on the targeting efficiency of ligand-functionalized nanoemulsions was investigated. We synthesized 100 nm nanoemulsions with a PEG surface density varying from 5 to 50 mol %. Fluorescent and paramagnetic lipids were included to allow their multimodal detection, while RGD peptides were conjugated to the PEG coating to obtain specificity for the $\alpha_v\beta_3$-integrin. The development of a unique experimental imaging setup allowed us to study, in real time, nanoparticle accumulation kinetics at (sub)-cellular resolution in tumors that were grown in a window chamber model with confocal microscopy imaging, and at the macroscopic tumor level in subcutaneously grown xenografts with magnetic resonance imaging. Accumulation in the tumor occurred more rapidly for the targeted nanoemulsions than for the nontargeted versions, and the PEG surface density had a strong effect on nanoparticle targeting efficiency. Counterintuitively, yet consistent with the PEG density conformation models, the highest specificity and targeting efficiency was observed at a low PEG surface density.

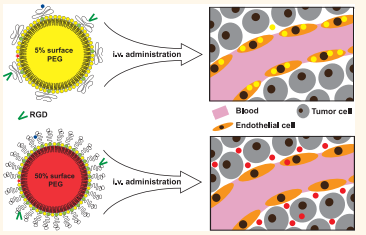

KEYWORDS: nanoemulsion · targeting-ligand · polyethylene glycol · surface density · intravital microscopy · dorsal window chamber · DCE-MRI

The use of nanoparticles for *in vivo* diagnostics and drug delivery has increased tremendously over the last two decades.[1,2] The exciting possibility of incorporating multiple functionalities within the same nanoparticle allows for *in vivo* monitoring of biodistribution and cargo delivery with a variety of imaging modalities.[3−5] Functionalization of the nanoparticles with targeting ligands, such as peptides[6] or aptamers,[7] has provided more control over *in vivo* nanoparticle distribution, and has enabled their use as molecular imaging agents.[3,8]

The pharmacokinetics and biodistribution of nanoparticles are to a large extent governed by their surface properties. Hence, a prerequisite for successful intravenous administration of nanoparticles is a suitable hydrophilic and biocompatible particle surface or surface coating. Such surface coatings can consist of polysaccharides,[9] poly(amino acids),[10] or synthetic polymers.[11] Within the latter class polyethylene glycol (PEG) was identified in the early nineties to be highly suitable[12−14] and has become the most widely used nanoparticle surface coating.[13−15] PEG is highly hydrophilic, has the lowest level of protein or cellular adsorption of any known polymer, is nontoxic, and many PEGylated therapeutics have been FDA-approved since its introduction.[1,14,15] Although the mechanism by which PEG coatings increase circulation times and improve biodistribution profiles is not fully understood, the most widely accepted explanation is that PEG provides a steric barrier, which prevents nanoparticle opsonization, thereby delaying removal from the circulation by the mononuclear phagocyte system (MPS).[14,15] A critical factor is the PEG density on the nanoparticle surface which has been found to modulate nanoparticle circulation times[16,17] and nonspecific cellular uptake.[18]

Nanoparticle targeting using cell surface receptor specific ligands, can enhance the

* Address correspondence to sjoerd.hak@ntnu.no.

Received for review April 13, 2012 and accepted May 28, 2012.

Published online June 06, 2012
10.1021/nn301630n

cellular uptake of nanoparticles.[19] However, a topic that remains largely uninvestigated is the effect PEG surface density has on the targeting potential of ligand-functionalized nanoparticles. Studies have shown that at low PEG density, the PEG units on a surface are organized in a so-called mushroom configuration, which transforms to a brush configuration at higher PEG density.[20] In the mushroom regime, no lateral interaction between neighboring polymers occurs, implying that the nanoparticle surface is not completely covered with PEG. In the brush regime the polymers overlap, fully covering the surface and providing optimal surface protection against opsonization. However, in the brush regime the lateral interactions between the polymers induce chain stretching outward from the nanoparticle surface, increasing the thickness of the PEG layer with increasing PEG density. A hypothesis is that when ligands are conjugated to the distal ends of the PEG chains in the brush confirmation, this interaction with neighboring PEG chains may reduce the ability of interaction with their molecular or cellular targets.

To investigate the above hypothesis, we developed a unique multimodal *in vivo* imaging setup which allowed us to study the effect of PEG surface density on target-specific nanoparticle accumulation in tumor tissue using both high resolution intravital microscopy and magnetic resonance imaging (MRI) on mice. The nanoparticle platform used is based on a recently introduced multimodal nanoemulsion,[21] of which the surface PEG-density can be judiciously varied. The $\alpha_v\beta_3$-integrin specific arginine-glycine-aspartic acid peptide RGD was used as a targeting ligand. $\alpha_v\beta_3$-integrin is highly expressed on angiogenically activated endothelial cells and is an extensively studied marker for tumor angiogenesis.[22] *In vitro*, $\alpha_v\beta_3$-integrin expressing human endothelial cells were used to study nanoemulsion targeting efficiency and cellular handling as a function of their PEG surface density. For *in vivo* experiments, we employed a dorsal window chamber tumor mouse model[23,24] and confocal laser scanning microscopy (CLSM) to evaluate nanoparticle targeting and accumulation in tumor tissue at a (sub)-cellular resolution in real time. Different fluorophores were used to distinguish targeted and nontargeted nanoparticles within the same tumor tissue, making this set up highly suitable to study the interactions between nanoparticles and the living tumor. Finally, to corroborate the CLSM observations on the whole tumor level with a clinically relevant imaging modality, dynamic contrast enhanced MRI (DCE-MRI) was explored to study the nanoemulsion tumor targeting dynamics.

RESULTS AND DISCUSSION

Nanoparticle Synthesis and Characterization. Nanoemulsions with six different PEG2000-DSPE contents (5, 10, 20, 30, 40, and 50 mol %, referred to as P5, P10, P20, P30, P40, and P50, respectively) were synthesized and characterized (Figure 1A), and all the components were incorporated at molar ratios as shown in Figure 1B. Increasing PEG2000-DSPE content resulted in a substantial decrease in nanoemulsion droplet size (data not shown). Plausibly this is due to PEG2000-DSPE having a very low critical packing parameter (~0.05), which reflects the dimensional proportion between the hydrophobic and hydrophilic part of an amphiphile.[25] Hence, in PEG2000-DSPE the hydrophilic polymer is very large relative to the hydrophobic fatty acid tails. This large hydrophilic polymer tends to increase the curvature of the membrane in which the lipid incorporates, decreasing the diameter of the particle. As nanoparticle size may have significant effect on cellular interaction and uptake,[26] the nanoparticle size was kept constant by increasing the amount of soybean oil with increasing PEG2000-DSPE content in the nanoemulsions (Figure 1B,C). The hydrodynamic diameters of the six nanoemulsions with different PEG content were approximately 100 nm with polydispersity indices (PDI) well below 0.2 (Figure 1C,D). The zeta potential of the nanoemulsions was below −25 mV, providing good colloidal stability caused by electrostatic repulsive forces between individual particles. The amino moiety in PEG-DSPE is negatively charged at neutral pH,[27] which was reflected by a more negative zeta potential for increasing PEG2000-DSPE content (Figure 1E). RGD conjugation increased the zeta potential slightly, which might be explained by shielding of the negative surface charge by the RGD peptides.[28] More detailed information about dynamic light scattering (DLS) results can be found in Table S1 in Supporting Information.

Cellular Uptake and Targeting As Function of PEG Content. To study the effect of PEG density on targeting efficiency, we used the $\alpha_v\beta_3$-integrin specific RGD peptide as a model targeting ligand. This integrin plays an important role in vascular angiogenesis for solid tumor growth and is significantly upregulated on angiogenically activated endothelial cells. Human umbilical vein endothelial cells (HUVEC) grown in culture are reported to express high levels of this integrin as well,[29] providing an *in vitro* model to study the targeting of the RGD conjugated nanoemulsions. HUVEC were incubated with medium containing either no emulsion (blank), or the RGD or nontargeted control (CTRL) version of the six formulations described above, and the cellular uptake was quantified using flow cytometry. For P5 and P10, RGD functionalization resulted in increased cellular uptake compared to uptake of CTRL nanoemulsions (Figure 2A,B). For P20, P30, P40, and P50 no difference between cellular uptake of targeted or nontargeted nanoemulsions was observed (Figure 2A,B). Furthermore, in the case of P5, P10, and P20, both targeted and nontargeted nanoemulsions internalized in 100% of the HUVEC, whereas for P30, P40, and P50,

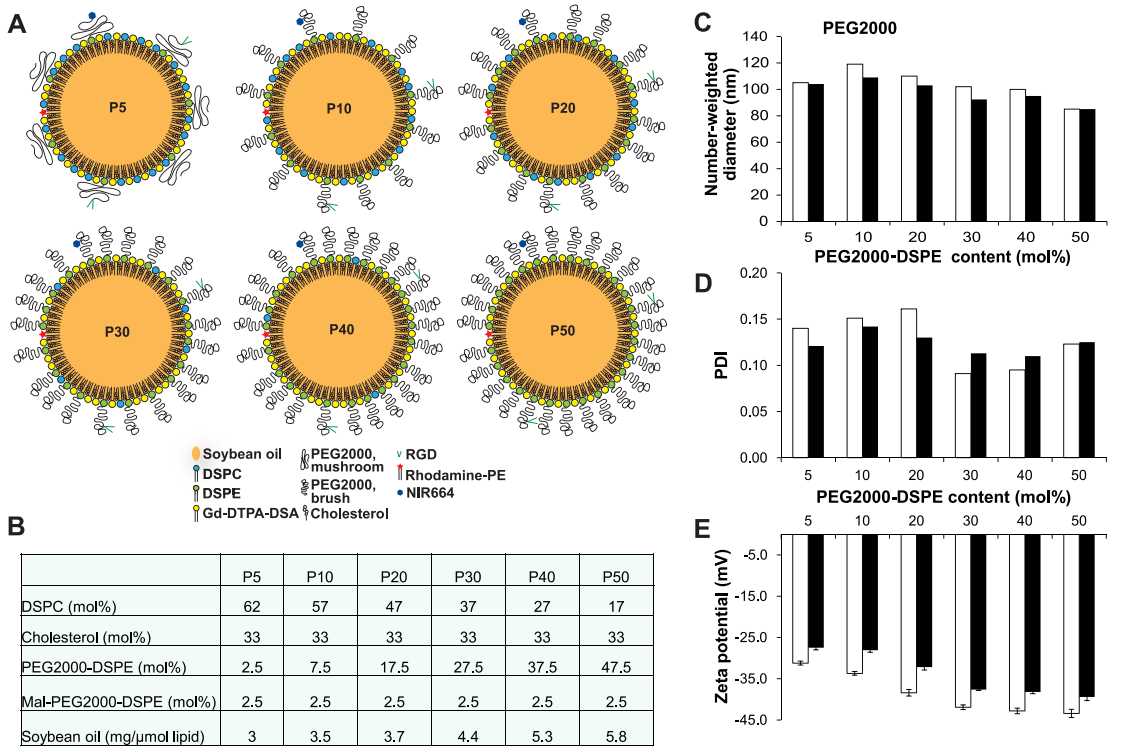

B

	P5	P10	P20	P30	P40	P50
DSPC (mol%)	62	57	47	37	27	17
Cholesterol (mol%)	33	33	33	33	33	33
PEG2000-DSPE (mol%)	2.5	7.5	17.5	27.5	37.5	47.5
Mal-PEG2000-DSPE (mol%)	2.5	2.5	2.5	2.5	2.5	2.5
Soybean oil (mg/μmol lipid)	3	3.5	3.7	4.4	5.3	5.8

Figure 1. Nanoemulsion schematics and characteristics. (A) Cartoons of the nanoemulsions with the different PEG2000-DSPE content and mushroom/brush configuration indicated. (B) Lipid and soybean oil content of the different nanoemulsions. (C) Hydrodynamic diameters of the nanoemulsions as a function of the PEG2000-DSPE content as measured with dynamic light scattering. (D) Polydispersity indexes (PDI) as a function of the PEG2000-DSPE content of the measured diameters as reported in panel C. (E) Zeta potentials as a function of the PEG2000-DSPE content. For panels C–E: white bars, CTRL nanoemulsion; black bars, RGD nanoemulsion.

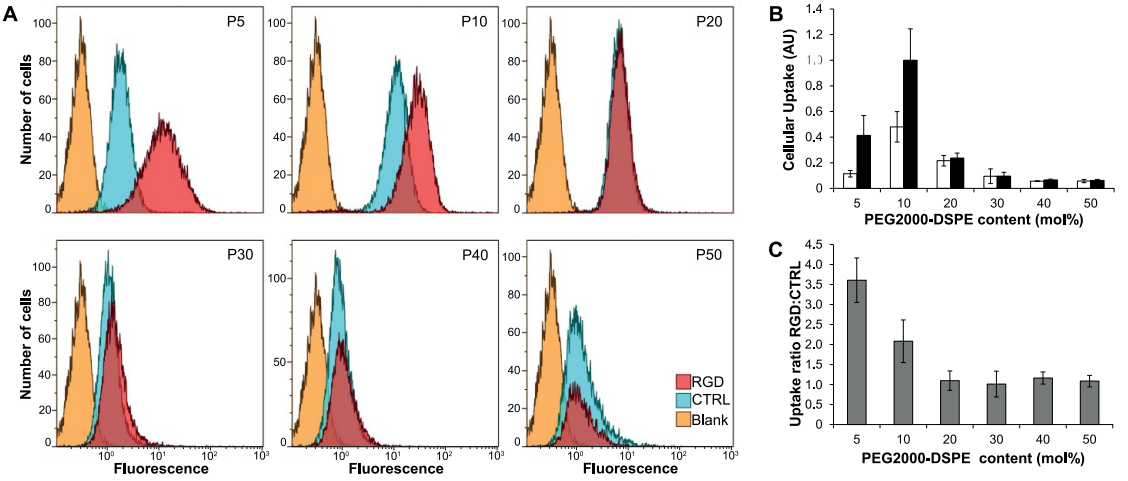

Figure 2. Cellular uptake as a function of PEG2000-DSPE content. (A) Logarithmic flow cytometry histograms for the nanoemulsions with the different PEG2000-DSPE content. (B) Normalized cellular uptake as the median fluorescence intensity of the positive cells divided by the median of the cellular autofluorescence for CTRL (white bars) and RGD (black bars) nanoemulsion. The error bars represent the standard deviation (n = 6). (C) Cellular uptake ratio between RGD and CTRL nanoemulsions. The error bars represent the standard deviation (n = 6).

only 60 to 90% of the cells internalized the nanoemulsion, indicating decreased nonspecific cellular interaction at higher PEGylation densities (Figure S1 in Supporting Information). The uptake ratio between RGD and CTRL nanoemulsions demonstrated that the targeting efficiency was highest at low PEG densities (P5 and P10) and virtually no targeting effect was observed at 20 mol % and higher PEG2000-DSPE densities (Figure 2C). Using the model published by Gennes *et al.*,[30] we calculated (section S1 in Supporting Information) that on P5, the PEG was predominantly present in a mushroom configuration, whereas in the

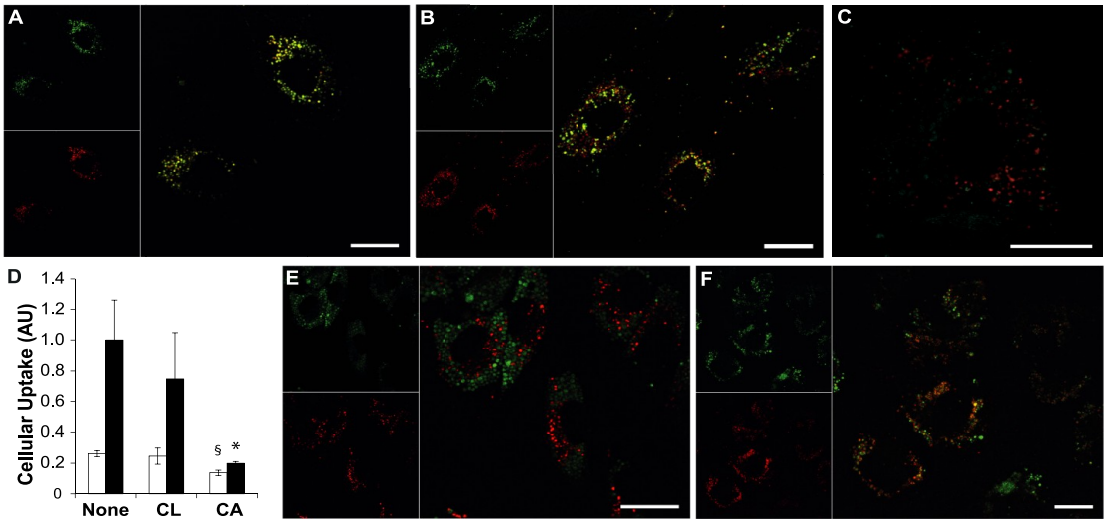

Figure 3. HUVEC incubated with P5 nanoemulsion for 3 h. White bars represent 20 μm. (A,B) RGD nanoemulsions (A) and CTRL nanoemulsions (B) which were double labeled with rhodamine-PE (green) and NIR664-PEG2000-DSPE (red). The 2 h postincubation RGD emulsions remained intact (yellow in overlay), whereas the CTRL emulsions partially disintegrated. (C) HUVEC simultaneously incubated with RGD nanoemulsion (red) and CTRL nanoemulsion (green) demonstrating different intracellular localization. (D) Cellular uptake for CTRL (white bars) and RGD (black bars) nanoemulsions when no endocytosis blocking was performed (None), when clathrin-dependent pathways were blocked (CL), and when caveolae-dependent pathways were blocked (CA). (§) CTRL None *vs* CA $p = 0.0001$ and (∗) RGD None *vs* CA $p = 0.004$). The error bars represent the standard deviation ($n = 4$). (E,F) HUVEC with lysosomes labeled in green incubated with RGD nanoemulsions (red in E) and CTRL nanoemulsions (red in F).

formulations with higher PEG densities, the polymer would be mostly present in the brush configuration, extending outward from the nanoemulsion surface. Taken together, this confirmed our hypothesis that high PEG surface densities inducing the brush configuration decrease the nanoparticle targeting efficiency.

Klibanov *et al*. observed that increasing the PEG5000-DSPE content up to 7 mol % in biotinylated liposomes progressively hampered their binding to avidin.[12] They conjugated biotin directly to the phosphate headgroups where they would readily be covered by surface-bound PEG. Although Klibanov *et al*. did demonstrate that nanoparticle PEGylation can affect ligand-directed nanoparticle targeting, it is likely that in such a configuration the PEG5000 interferes in the avidin−biotin binding in a similar fashion as in delaying opsonization. To circumvent this issue, Kirpotin *et al*. conjugated anti-HER2 Fab′ fragments to the distal ends of PEG chains in liposomes.[31] They observed no effect on the targeting efficiency of varying PEG2000 densities up to 5.7 mol %. This PEG density is what is maximally achievable for liposomes without affecting their morphology (obtaining micellular aggregates instead of liposomes),[32] and at this surface density no PEG brush conformation is induced. The unique features of our nanoparticle platform allow an increase of the PEG surface density up to 50% and thus lets us study the influence of PEG on ligand targeting in both a wider range of densities and at densities high enough to induce the brush regime. Another possible explanation for why Kirpotin *et al*. did not detect effects of PEG density on targeting is that due to the large size of the Fab fragment (∼55000 g/mol) compared to both RGD (720 g/mol) and the PEG polymer used (2000 g/mol), the PEG coating may have less effect on ligand-target interactions.

Cellular Uptake Mechanism and Intracellular Trafficking. The cellular uptake and intracellular trafficking of the RGD and CTRL nanoemulsions were studied by live cell CLSM as a function of PEG surface density. To study particle integrity after internalization, the P5, P10, and P20 nanoemulsions were double labeled with two spectrally different fluorochromes conjugated to two different lipids; rhodamine-PE and NIR664-PEG2000-DSPE. In the case of rhodamine-PE, rhodamine is directly conjugated to the PE headgroup, whereas NIR664 is conjugated to the distal end of PEG in NIR664-PEG2000-DSPE. Importantly, as those two lipids differ significantly in their molecular structure, they could be expected to be trafficked differently when the nanoemulsions disintegrate intracellularly. For P5 it was found that in the first two hours after incubation with the nanoemulsion, the fluorescence from the two different lipids generally colocalized, in the case of RGD nanoemulsion, but was more separated in the case of CTRL nanoemulsions (Figure 3A,B). This demonstrated that the RGD functionalization had a significant effect on the intracellular fate of the nanoemulsions. The RGD nanoemulsions were internalized intact and stayed mostly intact up to 2 h after incubation, whereas the CTRL nanoemulsions were mostly disintegrated immediately upon internalization. In the case of P10 and P20, no differences in integrity of the RGD and CTRL nanoemulsions could be detected, both the RGD

and CTRL nanoemulsions seemed partially disintegrated during the first 2 h after internalization (Figure S1 in Supporting Information). At these higher PEG surface densities, the RGD nanoemulsions behaved similar to nonspecific CTRL nanoemulsions, an observation which was also reflected by the poor targeting at higher surface PEG density found by flow cytometry measurements (Figure 2C). Therefore the following *in vitro* experiments were done with P5 nanoemulsions.

To study whether the difference in integrity for P5 RGD and CTRL nanoemulsion could be related to different intracellular localization, HUVEC were coincubated with RGD and CTL nanoemulsions labeled with, respectively, NIR664-PEG-DSPE and rhodamine-PE. Minimal colocalization between the RGD and CTRL nanoemulsions was observed in the first 2 h after incubation, confirming different intracellular localization and potentially different internalization mechanisms (Figure 3C). Endocytic pathways were studied by utilizing inhibitors of clathrin- and caveolae-mediated endocytosis. HUVEC were incubated with nanoemulsions in the presence of the inhibitors, and cellular uptake was subsequently quantified by flow cytometry (Figure 3D). For P5 RGD nanoemulsions a slight, but not statistically significant, reduction in cellular uptake was observed when clathrin-mediated endocytosis was inhibited (approximately 25% reduction, $p = 0.131$). Inhibition of caveolae-dependent pathways resulted in approximately 80% reduction in cellular uptake ($p = 0.004$), indicating that the RGD nanoemulsions were mainly internalized through a caveolae-dependent pathway. This is consistent with the reports that $\alpha_v\beta_3$-integrin can be internalized *via* caveolae-mediated endocytosis.[33]

Similar results were obtained for the CTRL nanoemulsion; however, the differences were less pronounced. The CTRL nanoemulsion was hardly internalized *via* clathrin-dependent pathways, but mainly through the caveolae-dependent pathway (clathrin-mediated endocytosis inhibition, approximately 10% reduction in uptake with $p = 0.305$; caveolae-dependent endocytosis inhibition, approximately 50% reduction in uptake with $p = 0.0001$). Hence, as the inhibition of caveolae-dependent pathways decreased cellular uptake by only 50%, other caveolae- and clathrin-independent pathways are probably involved in cellular entry of the CTRL nanoemulsions as well.

Various intracellular destinations such as endoplasmatic reticulum, Golgi apparatus, endosomes, and lysosomes have been observed for material internalized *via* a caveolae-dependent pathway.[34] Thus, we labeled lysosomes with lysotracker, which stains acidic compartments such as late endosomes and lysosomes, to study the colocalization between lysosomes and nanoemulsions. A clear difference in association between lysosomes and the RGD and CTRL nanoemulsions was observed (Figure 3E,F). The P5 CTRL nanoemulsions mostly colocalized with lysosomes shortly after incubation, whereas the RGD nanoemulsions showed little association with the lysosomes in the first 2 h after internalization. These results are in agreement with the findings of Oba *et al.* studying the internalization mechanism and lysosomal colocalization of RGD-conjugated and nonconjugated PEG–polylysine–DNA polyplexes.[35,36] They also found that the RGD-conjugated nanoparticles internalized in a caveolae-dependent manner, colocalized with lysosomes to a lower extent than nontargeted nanoparticles, and predominantly localized to perinuclear regions. Thus, the RGD–peptide caused a different intracellular route for the targeted nanoemulsions than for nontargeted nanoemulsions. CTRL nanoemulsions seemed to follow the classical route from early endosomes to late endosomes and lysosomes, whereas the RGD nanoemulsions were shown to escape this route. It is known that $\alpha_v\beta_3$-integrin is localized in caveolae and that after internalization it is recycled back to the plasma membrane *via* various routes.[37] These integrin recycling routes bypass lysosomes, which may explain that the transport to late endosomes and lysosomes of RGD nanoemulsions was avoided. Moreover, certain viruses[38] and bacteria[39] have been found to enter cells in a receptor-mediated caveolae-dependent manner and avoid lysosomal degradation as well. As lysosomes constitute the intracellular digestion compartment, the observed colocalization between lysosomes and CTRL nanoemulsions explain the disintegration of the CTRL nanoemulsions upon cellular entry as opposed to the RGD nanoemulsions, which stayed intact after internalization.

Intravital CLSM. To study *in vivo* vascular targeting efficiencies, we employed a tumor model growing in dorsal window chambers in mice. This model allows intravital CLSM, providing real time imaging of nanoemulsion dynamics and localization at a subcellular resolution. Employing spectrally different fluorescent labels for simultaneously administered CTRL and RGD-functionalized nanoemulsion, this model offers the exciting possibility to study the tissue distribution of both nanoemulsions in the same tumor tissue, excluding individual differences affecting the observations. *In vitro,* we found that 5 mol % PEGylation resulted in optimal targeting efficiency. However, a recent study has shown that RGD conjugated nanoemulsions containing 50 mol % PEG2000-DSPE exhibited specificity for the tumor vasculature.[40] Thus, vascular targeting of both P5 and P50 nanoemulsions were studied *in vivo*.

P5 RGD nanoemulsions were confined to the vessel wall, and essentially no extravasation was observed approximately 6 h post injection (Figure 4A,B), demonstrating high affinity for the tumor vasculature. At the same time point, the P5 CTRL nanoemulsion hardly accumulated in the vessel wall, but extravasated from the tumor vasculature (Figure 4A,B). Simultaneous

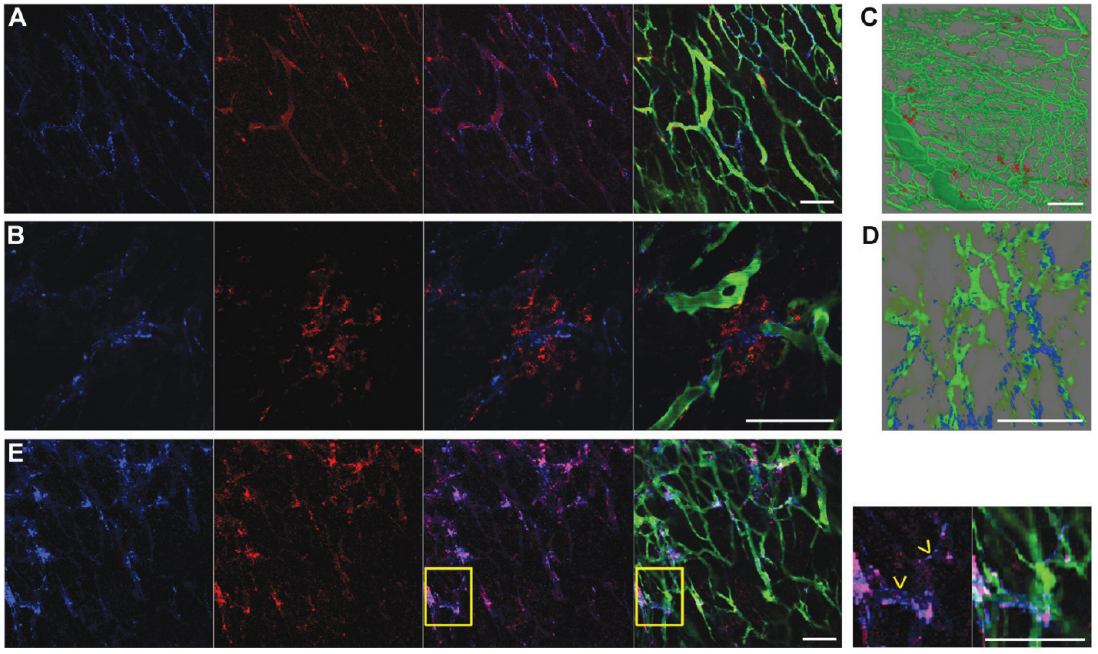

Figure 4. Nanoemulsion distribution imaged by intravital microscopy. Images obtained after injection of P5 nanoemulsions (A–D) and P50 nanoemulsions (E). RGD nanoemulsion in blue, CTRL in red, and the vasculature in green. Scale bars represent 100 μm. (A) At 6 h postinjection, the P5 RGD nanoemulsion was confined to the vessel wall, whereas the CTRL nanoemulsion extravasated. (B) A region with extensive extravasation of the P5 CTRL nanoemulsion, where the P5 RGD nanoemulsion was confined to the vessel wall 6 h post injection. (C,D) 3D reconstructions from *z*-stacks obtained 4 h postinjection of P5 RGD nanoemulsion (C) and 8 h postinjection of P5 CTRL nanoemulsion (D). (E) At 6 h postinjection of P50 nanoemulsions the distribution of the RGD and the CTRL nanoemulsions was very similar as evident from the pink color in the overlay. In the magnified insets the arrows indicate RGD nanoemulsion localizing to the vessel wall.

injection of the differently fluorescently labeled CTRL and RGD nanoemulsions, demonstrated that at spots where the CTRL nanoemulsions displayed extensive extravasation (Figure 4B), being indicative for high vascular permeability, the RGD nanoemulsions were restricted to the vessel wall (Figure 4B). This confirmed that the P5 RGD nanoemulsions selectively target the angiogenic tumor vasculature. Previous studies have also demonstrated that RGD multivalency directs nanoparticles to angiogenic endothelial cells and restricts extravasation.[41,42] 3D reconstructions of *z*-stacks obtained intravitally showed that throughout the imaged volumes, RGD nanoemulsions remained relatively homogeneously confined to the vessel wall, whereas CTRL nanoemulsions extravasated from the vasculature in a more heterogeneous manner (Figure 4C,D and Figure S2 in Supporting Information).

For P50, only a minor targeting effect was observed approximately 6 h postinjection. In mice injected with spectrally different RGD and CTRL P50 nanoemulsion, the agents were distributed very similarly throughout the tumor tissue as demonstrated by the high degree of colocalization of the two agents (Figure 4E). Although this indicated nonspecific association of the CTRL nanoemulsions with the vessel wall and extravasation of RGD nanoemulsion, the RGD nanoemulsions colocalized with the vessel wall to a slightly higher extent, as illustrated in the magnified insets in Figure 4E. Although this demonstrated some specificity of P50 for the tumor vasculature, our main conclusion is that these *in vivo* results confirmed the *in vitro* observation that targeting of the nanoemulsions is most efficient at low surface PEG density and that at high PEG surface density the RGD nanoemulsions behave very similar to CTRL nanoemulsions.

Studying the tissue accumulation kinetics of the RGD and the CTRL agents, it was found that the P5 RGD nanoemulsions started to accumulate in the vessel wall within 10 min postinjection, as shown by a speckeled pattern colocalized with the vessel wall, which persisted to 30 min postinjection (Figure 5A). In addition to the speckled pattern, the nanoemulsion was clearly observable inside the vasculature at these early time points. At 2 h postinjection, less circulating nanoparticles were observed, and the vessel wall had become highly fluorescent resulting in a distinct delineation of the tumor vasculature, which remained clearly visible up to 24 h postinjection (Figure 5A). Hence, the accumulation of the P5 RGD nanoemulsions started upon injection and the particles accumulated and remained in the vessel wall throughout the imaging period. In the case of the P5 CTRL nanoemulsion, only few of the inspected tumor regions contained extravasated nanoemulsions within the first 30 min postinjection, visible as high fluorescence intensity foci, and probably only in regions with high vascular permeability (Figure 5B). At 2 to 4 h after injection some regions showed clear extravasation; however, other regions remained without

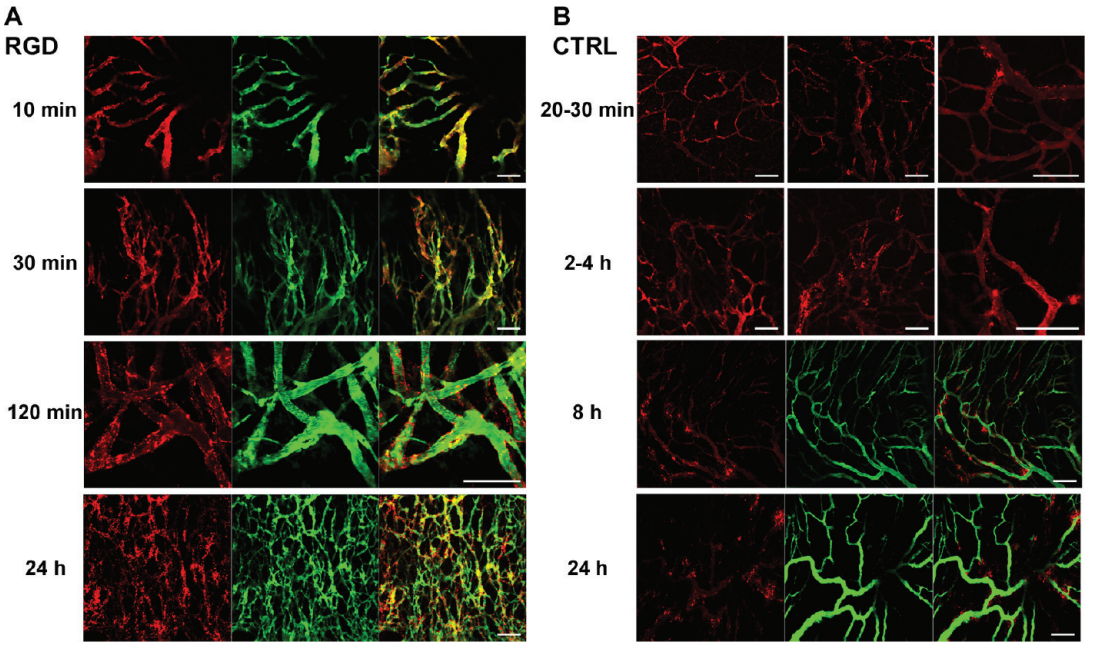

Figure 5. P5 nanoemulsion accumulation kinetics imaged by intravital microscopy. Nanoemulsions in red and the vasculature in green. White bars represent 100 μm. (A) Already at 10 and 30 min postinjection of RGD nanoemulsions, a speckled accumulation pattern was observed and 2 h postinjection and onward a clear binding to the vasculature wall occurred. (B) Up to 4 h postinjection, the extravasation of CTRL nanoemulsion was very heterogeneous as shown in the multiple images at those time points. Regions with significant accumulations and extravasation, visible as high fluorescence intensity foci, and also regions with hardly any fluorescence were observed. At 8 h postinjection and onward the CTRL nanoemulsion had extravasated throughout the tumor.

any detectable accumulation of the agent. It was not before approximately 8 h postinjection that the majority of the tumor contained significant quantities of extravasated nanoemulsion, which persisted up to 24 h postinjection (Figure 5B). Taken together, the P5 RGD nanoemulsions accumulated both faster and in a more homogeneous manner in the tumor tissue than the P5 CTRL nanoemulsions.

The P50 nanoemulsions displayed similar dynamics as the P5 nanoemulsions (Figure S3 in Supporting Information): faster accumulation of the RGD nanoemulsions than of the CTRL nanoemulsions. However, significant extravasation of both P50 agents was observed at later time points and as pointed out earlier, the specificity for the vessel wall of the P50 RGD nanoemulsions was substantially lower than that of P5 RGD nanoemulsions.

DCE-MRI. With the subcellular resolution of the intravital CLSM it was possible to demonstrate pronounced differences for particle distribution and accumulation dynamics of the P5 RGD and CTRL nanoemulsions. However, it did not provide information on the particle behavior on the whole tumor level. For this purpose we used MRI. First we investigated whether it was possible to detect the cellular uptake of the nanoemulsions with MRI *in vitro*. HUVEC were incubated with medium containing either no (blank) or RGD or CTRL P5 nanoemulsions labeled with gadolinium (Gd-DTPA-DSA). After thorough washing, cell pellets were formed and imaged with a T_1-weighted protocol including quantification of T_1 relaxation times (Figure 6A,B). A pronounced decrease in T_1 relaxation times of cell pellets incubated with the paramagnetic nanoemulsions was found. However, the decrease in T_1 relaxation times was most pronounced in the cell pellets incubated with the RGD version. The Gd concentration in cells was calculated, based on an ionic relaxivity of 3.2 mM^{-1} s^{-1}, as we measured at 7 T and room temperature, and the uptake ratio between RGD and CTRL nanoemulsions was found to be very similar to the uptake ratio determined by flow cytometry. This demonstrated that our P5 nanoemulsions are observable with MRI and that relative quantification of the nanoparticle uptake with MRI is feasible *in vitro*.

MRI and other clinical imaging modalities lack the spatial resolution to readily discriminate between contrast agent binding to the tumor endothelium and contrast agent extravasation to the tumor interstitium in static images. As the intravital CLSM not only demonstrated differences in the nanoemulsion distribution, but also showed a distinct difference between the dynamics of the CTRL and the RGD nanoemulsions, we explored DCE-MRI for its ability to study the dynamics of the nanoemulsions on the whole tumor level and thereby corroborate the CLSM findings.

The thin tumors in the dorsal window chamber do not allow MRI at sufficient signal-to-noise ratio. Therefore we used ovarian cancer xenografts growing subcutaneously on the flank of mice for the DCE-MRI. The P5 nanoemulsions were injected intravenously, and

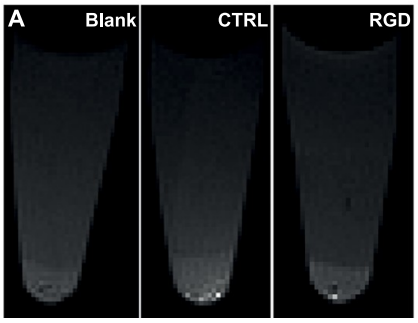

B

	T_1 ± SD (ms)	R_1 (1/s)	Gd (mM)	Uptakeratio RGD:CTRL
Blank	2198± 98.8	0.455	0	-
CTRL	2002± 17.2	0.499	0.014	-
RGD	1677± 27.6	0.596	0.044	3.2

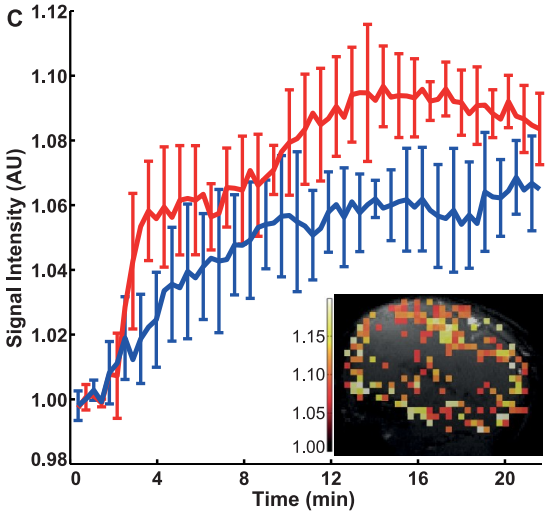

Figure 6. MRI results obtained with P5 nanoemulsion containing Gd-DTPA-DSA. A: T1-weighted images of pellets of HUVEC incubated with either no (blank), or RGD or CTRL nanoemulsion. (B) T1 and R1 (1/T1) values in the cell pellets (n = 3) and the calculated cellular Gd concentration. The uptake ratio was determined by dividing the Gd concentration in RGD incubated pellets by the Gd concentration in CTRL incubated pellets. (C) DCEMRI curves in the tumor rim in mice injected with CTRL nanoemulsion (blue, n = 3) or RGD nanoemulsion (red, n = 3). The error bars represent the standard deviations. The inset shows a high resolution T1-weighted image of a tumor on a mouse flank obtained 25 min post-RGD nanoemulsion injection. The color coded overlay shows the relative signal intensity in the DCE-MRI in the same units as the curves.

the tumor was imaged at a temporal resolution of 21.6 s over the time course of 20 min. Signal enhancement in the tumor during the DCE-MRI predominantly occurred in the tumor rim, whereas the core region of the tumor displayed limited signal increase (inset in Figure 6C). It has also been shown that in solid tumors, $\alpha_v\beta_3$-integrin expression by vascular endothelial cells is predominantly occurring at the tumor rim.[41] Therefore, the signal intensity *versus* time curve from the DCE-MRI was obtained from ROIs containing only the tumor rim. These curves showed a clear difference between the dynamics of the RGD and the CTRL nanoemulsions. For both nanoemulsions an increase in signal intensity was observed, however for the RGD nanoemulsions the increase was larger (Figure 6C). Additionally, the signal intensity increased faster for the RGD nanoemulsion, reflecting the more rapid accumulation of the RGD nanoemulsions as was observed in the intravital CLSM. This not only confirmed that the different dynamics of the RGD and the CTRL nanoemulsions as was observed in the intravital CLSM experiments occurred throughout the angiogenic tumor rim, but also demonstrated that DCE-MRI can become a potent tool to study the targeting efficacy of targeted MRI contrast agents *in vivo*. Actually, recently, the first studies employing dynamic MRI techniques to study the dynamics of nanoparticles targeted to the tumor vasculature have appeared.[43,44] Oostendorp *et al.* used a paramagnetic nanoparticle and also observed their targeted agent to accumulate both faster and in larger amounts in the tumor rim in the first 20 min postinjection.[43]

As the DCE-MRI curves mainly reflect the dynamics of two processes, namely blood clearance of the agent, which causes a reduction in signal intensity, and increasing contrast agent concentration in the tumor, which increases the signal intensity, absolute quantification of $\alpha_v\beta_3$-integrin expression levels is not straightforward. Furthermore, the accumulation of the RGD nanoemulsions is not necessarily solely occurring *via* integrin targeting, but might partially occur also through nonspecific processes. Moreover, the nanoemulsions are likely to change their relaxivity upon accumulation in the tissue, further complicating quantification. However, the present approach can be used to qualitatively assess $\alpha_v\beta_3$-integrin expression, which would be a useful tool in monitoring response to antiangiogenic therapy in both preclinical and clinical settings.

CONCLUSION

We developed a multimodal nanoparticle system in which the PEG surface density can be judiciously varied. Employing this nanoparticle platform and a unique combination of real time intravital microscopy and DCE-MRI allowed us to systematically investigate the effect of PEG surface density on *in vivo* nanoparticle behavior. Specifically, in this study we investigated the effect of PEG surface density on the targeting potential of ligand-functionalized nanoparticles. Intravital microscopy provided real-time information on nanoparticle targeting to the angiogenic tumor vasculature at the cellular level, while DCE-MRI could be used to study targeting kinetics at the macroscopic tumor level. Tumor accumulation occurred much faster for the targeted nanoemulsions than for the nontargeted versions. Counterintuitively, yet consistent with the PEG density conformation models, both the *in vitro* and *in vivo* studies demonstrated that a low PEG surface density, at which the PEG chains are present in a

mushroom configuration, was optimal for efficient and specific nanoparticle targeting. Therefore, we conclude that the optimal PEG surface density for peptide conjugated nanoparticle systems around 100 nm in size should be set below 10%. Conveniently, typical nanoparticle PEG surface densities used to improve nanoparticle pharmacokinetics and biodistribution are within this range. This is crucial knowledge in the quest for the optimal design of ligand-functionalized nanoparticles.

MATERIALS AND METHODS

Nanoparticle Synthesis. Stock solutions of all the components in chloroform were prepared. Typically a total of 20 μmoles of the amphiphillic lipids (1,2-distearoyl-*sn*-glycero-3-phosphocholine (DSPC), cholesterol, 1,2-distearoyl-*sn*-glycero-3-phosphoethanolamine-*N*-[methoxy(polyethylene glycol)-2000 (PEG2000-DSPE), maleimide-PEG2000-DSPE, purchased from Avanti Polar Lipids) were mixed at molar ratios as indicated in Figure 1B. The amount of soybean oil was defined as milligram per micromole of the amphiphillic lipid mixture. For fluorescence imaging, 0.1 mol % of NIR664-PEG2000-DSPE (SyMO-Chem) and/or 1,2-dipalmitoyl-*sn*-glycero-3-phosphoethanolamine-*N*-lissamine rhodamine B sulfonyl ammonium salt (rhodamine-PE, Avanti Polar Lipids) was added, and for MRI 25 mol % gadolinium-diethylenetriaminepentacetate-bis(stearylamide) (Gd-DTPA-DSA, Avanti Polar Lipids) was added at the expense of DSPC. Subsequently the chloroform was evaporated with rotation evaporation (60 min at maximum vacuum and room temperature)m, and the resulting lipid film was hydrated with hepes buffered saline (HBS, 2.38 g/L Hepes and 8 g/L NaCl, pH 6.7). The obtained crude emulsion was sonicated for 20 min (Heat Systems-Ultrasonics, W-225R, duty cycle 35%, 30 W and 20 kHz) in a water bath keeping the emulsion at ambient temperature. Half of the final nanoemulsions were conjugated with c(RGDf(-S-acetylthioacetyl)K) (Ansynth) (RGD, 13.5 μg RGD per μmole lipid). Before adding the peptide to the maleimide functionalized nanoemulsion, the thiol group on the RGD peptide was deacetylated at pH 7 for 1 h. The activated peptide was added to the nanoemulsions and the resulting mixture was left to react overnight at 4 °C. The nanoemulsions were concentrated when necessary with vivaspin concentrators (100 kDa MWCO) and finally dialyzed (Spectra/Por Float-A-Lyzer G2, 100 kDa MWCO, Spectrum Laboratories) against HBS of pH 7.4 to remove unconjugated RGD and to obtain physiological pH. After preparation, the nanoemulsions were stored at 4 °C for a minimum of 5 days before using them in experiments to ensure hydrolysis of unreacted maleimide groups.

Dynamic Light Scattering and Zeta Potential Measurement. The hydrodynamic size and size distribution, and the zeta potential were measured using dynamic light scattering techniques (Malvern, Zetasizer Nano PS). For size measurements, 8 μL of nanoemulsion suspension was dispersed in 800 μL HBS in an ordinary cuvette. Reported values were the average of approximately 50 measurements. The reported values are the means and PDIs after combining the 50 measurements with the Malvern zetasizer series software. For zeta potential measurements 20 μL of nanoemulsion suspension was dispersed in 1.5 mL of dH_2O in a capillary cell (Malvern, DTS1061). Reported values were the average of 300 measurement runs.

Cell Culturing and Incubations. HUVEC (Lonza Bioscience) were cultured in gelatin coated cell culture flasks using Dulbecco's modified eagle medium (DMEM, Gibco/Invitrogen) supplemented with endothelial cell growth medium (EGM) BulletKit (1% FBS, Lonza Bioscience). The cells were used for experiments at passage 4 to 7. In all experiments, the cells were incubated in medium containing either no (blank), RGD, or CTRL (nontargeted) nanoemulsions at a 1 mM lipid concentration for 3 h, followed by washing 3 times with PBS. For live cell imaging with CLSM, HUVEC were grown in gelatin coated 8-well μ-slides (Ibidi). After the incubation and washing, the cells were maintained in fresh medium. For flow cytometry experiments, HUVEC were grown in gelatin-coated 12-well plates. After nanoemulsion incubation, the cells were detached from the wells with 0.25% trypsin-EDTA solution (Sigma-Aldrich), spun down at 1500 rpm for 5 min, resuspended in ice cold PBS, and placed on ice. In the endocytosis inhibition assay, the cells were preincubated with either chlorpromazine (10 μg/mL) or genistein (70 mg/mL) for 30 min before incubation with medium containing both the endocytic inhibitor and the nanoemulsions.

Flow Cytometry. Cellular uptake of nanoemulsions was measured by flow cytometry (Gallios, Beckman Coulter). The 633 nm laser line was used to excite the NIR664 fluorochrome and the fluorescence was detected using a 650−670 bandpass filter. The flow cytometry data were analyzed using the software Kaluza (Beckman Coulter). Cellular fragments and debris were excluded from the analysis by gating the fluorescence on the side scatter *vs* forward angle light scatter signal. Within one experiment all the samples were analyzed using the same gate. The cellular uptake was measured both as the percentage of cells with higher fluorescence intensity than cellular autofluorescence as well as the amount of internalized nanoemulsion, which was estimated as the median fluorescence intensity divided by the median of the autofluorescence and normalized to the observed maximum cellular uptake. The targeting effect was defined as the ratio between the normalized fluorescence intensity of cells incubated with RGD or CTRL nanoparticles.

Live Cell CLSM. Live HUVEC were imaged by CLSM (Zeiss LSM 510 META) using an apochromate 40×/1.2 water immersion objective and a frame size of 1024 × 1024 pixels. The 8-well μ-slide was placed in an incubation chamber (PECON, CTI-controller 3700 and temp control 37-2) mounted on the CLSM object stage, and the cells were imaged at 37 °C and 5% CO_2. NIR664-PEG-DSPE was excited at 633 nm, the fluorescence was detected using a meta-detector at 676−719 nm, and rhodamine-PE was excited at 543 nm and detected using a meta-detector 569−612 nm.

To assess particle integrity, the cells were incubated with P5, P10, and P20 CTRL and RGD nanoemulsions containing both NIR664-PEG-DSPE and rhodamine-PE and imaged up to 3 h post incubation.

Intracellular localization of the P5 RGD and CTRL nanoemulsions were compared by coincubating the cells with CTRL nanoemulsions labeled with rhodamine-PE and RGD nanoemulsions labeled with NIR664-PEG2000-DSPE.

To assess lysosome colocalization of the nanoemulsion, the cells were incubated for 45 min with medium containing 50 nM lysotracker green (Invitrogen) and washed before the incubations with nanoemulsions. Lysotracker green was excited at 543 nm and detected at 565−615 nm

Intravital CLSM. For intravital CLSM, tumors grown in dorsal window chambers in mice were used. The window chambers (made of polyoxymethylene, built in house) were implanted as previously described[45] in male athymic Balb/c Nu/nu mice of 20 to 25 g. The mice were anesthetized with a subcutaneous injection of 12 mg/kg midazolam/fentanyl/haloperidol/water (3/3/2/4). At 24 h after implanting the chambers, $2-3 \times 10^6$ HeLa cells (from the cell line of human cervical carcinoma cells) were injected in the center of each chamber. The surgical procedures were performed under sterile conditions. The animals were kept under pathogen-free conditions at a temperature of 19 to 22 °C, 50 to 60% humidity, and 65 air changes per h, and animals were allowed food and water *ad libitum*. The drinking water contained 2% sucrose and 67.5 mg/L Baytril (enrofloxacin). After 12−16 days when the tumors were 0.2 to 0.7 cm thick and filled 30 to 100% of the window area, the mice were used for experiments. The mice were anesthetized by subcutaneous injections of 12 mg/kg midazolam/fentanyl/Haldol/water (3/3/2/4) and either P5 or P50 nanoemulsions

were intravenously (iv) injected at a dose of 80 μmole lipid/kg bodyweight. Six mice received each PEG formulation and from these two mice received RGD (NIR664-PEG-DSPE labeled), two mice received CTRL (NIR664-PEG-DSPE labeled), and two mice received both RGD (rhodamine-PE labeled) and CTRL (NIR664-PEG-DSPE labeled) nanoemulsions. This allowed us to study the distribution of each agent in four mice. For visualization of the vasculature, 100 μL of 20 mg/mL 2MDa FITC labeled Dextran (Sigma-Aldrich) was injected iv. The anesthetized mice were placed on a heating pad at 37 °C which was fixed to the microscope stage in a specially designed mouse holder. The tumors were imaged using a C-Apoplan 40x/0.8 water objective with long working distance. NIR664 and rhodamine were excited and detected as for imaging of cells. FITC-dextran was excited at 488 nm and detected with a bandpass filter at 500−550 nm. The tumors were imaged from the coverslip and approximately 100 μm into the tissue with a frame size of 512 × 512 pixels. 3D visualizations of intravitally acquired *z*-stacks were obtained using Amira (Visage Imaging)

MRI. All the MRI experiments were performed in a Bruker Biospec 7.05 T horizontal bore magnet. The T_1 relaxivity of the Gd in the nanoemulsions was obtained using a dilution series in HBS (pH 7.4) of six different Gd concentrations ranging from 0.05 to 1 mM in 2 mL of eppendorf tubes. The tubes were placed in an in house built sample holder which was imaged with a volume resonator. The T_1 relaxation time was measured using a spin−echo protocol: echo time (T_E) of 8.4 ms; repetition times (T_R) of 15, 25, 50, 75, 100, 200, 300, 400, 600, 800, 1200, 1600, 3200, 6400, 12800, 18000 ms; field of view (FOV) of 60 × 40 mm^2; matrix (MTX) of 128 × 128; slice thickness of 2 mm; 2 averages.

For P5 nanoemulsion detection *in vitro* in cell pellets, HUVEC were incubated with nanoemulsions for 3 h (n = 3 in each group: blank, RGD nanoemulsion, and CTRL nanoemulsion), washed, and detached with trypsin. The cell suspension was centrifuged and the pellet fixed with 150 μL of 4% paraformaldehyde and transferred to a 200 μL eppendorf tube. In the eppendorf tube a cell pellet was formed by gravity. The cell pellets were imaged using a quadrature surface coil with a T_1-weighted spin echo sequence: T_E of 7.7; T_R of 1000 ms; FOV of 20 × 16 mm^2, MTX of 100 × 80, slice thickness of 0.5 mm; 20 averages. Subsequently a T_1-map was obtained with a spin echo protocol: T_E of 8.4 ms; T_R of 42, 80, 160, 320, 640, 1280, 2000, 3500, 5000, 8000, 12000, 16000 ms; FOV of 16 × 16 mm^2; MTX of 80 × 80; slice thickness of 0.6 mm; 4 averages.

For DCE-MRI, the xenografts of the ovarian cancer cell line TOV21G in 12 week old female athymic Balb/c Nu/nu mice were used. Tumors were imaged around 4 weeks after subcutaneous inoculation of 1.5 × 10^6 tumor cells in the flank. The animals were kept under pathogen-free conditions at a temperature of 19 to 22 °C, 50 to 60% humidity, and 65 air changes per h, and animals were allowed food and water *ad libitum*. The mice were anesthetized with isoflurane (2% in 67% N2/33% O2) and the tail vein was canulated. Respiration rate and body temperature were monitored using pressure-sensitive and rectal temperature probes (SA Instruments, New York, NY, USA) and hot air flow and isoflurane flow were adjusted accordingly. The tumors were imaged with a quadrature surface coil using a dynamic imaging sequence with a temporal resolution of 21.6 s and using 60 repetitions it lasted 21.6 min (RARE pulse sequence with T_E of 7 ms; T_R of 300 ms, RARE factor 2, zero filling acceleration of 1.34, FOV25.2 × 14.4 mm, MTX of 56 × 32, slice thickness of 1 mm, 1 slice, 6 averages). The nanoemulsions were injected iv at the start of the 11th repetition as a bolus lasting approximately 20 s. Either P5 RGD nanoemulsions (n = 3) or P5 CTRL nanoemulsions (n = 3) were injected at a dose of 80 μmole of lipid/kg bodyweight, resulting in 20 μmole Gd per kg bodyweight. In the frames with the highest relative signal enhancement in the DCE-MRI, pixels in the tumor with at least 6% relative signal enhancement were color coded using Matlab (The MathWorks, Natick, MA, USA). Those color-coded relative signal enhancement maps were merged with high resolution T_1-weighted postinjection images to visualize the distribution of signal enhancement throughout the tumor. The high resolution T_1-weighted images were obtained 25 min post-nanoemulsion injection (FLASH pulse sequence, T_E of 5.4 ms, T_R of 350 ms, FOV 25.2 × 14.4 mm, MTX of 56 × 32, slice thickness of 1 mm, 1 slice, 4 averages). Those images were also used as a reference when defining ROIs in the dynamic sequence. The analysis of the T_1-maps and the DCE-MRI curve plotting was performed using Matlab.

Statistical Analysis. Where appropriate, statistical testing was performed using 2 sample, upper tailed student t tests with Minitab software (Minitab Inc., State College, PA, USA). The significance criterion was $p \leq 0.05$.

Conflict of Interest: The authors declare no competing financial interest.

Acknowledgment. We gratefully thank K. Sæterbø for implanting the dorsal window chambers in mice and culturing cells, S. Andersen, K. Pettersen, and S. Moerstue for providing and taking care of the mice with subcutaneous xenografts used in the *in vivo* MRI experiments, Ø. Risa and M. Thuen for their help with the MRI experiments, and P. Goa for help with MRI data analysis. The work was supported by the Norwegian Cancer Society, Medical Imaging Laboratory (MI-lab, NTNU, Norway), and the NIH Grant R01 CA155432 (W.J.M.M.).

Supporting Information Available: Supporting figures and calculations are provided in the Supporting Information. This material is available free of charge *via* the Internet at http://pubs.acs.org.

REFERENCES AND NOTES

1. Wagner, V.; Dullaart, A.; Bock, A. K.; Zweck, A. The Emerging Nanomedicine Landscape. *Nat. Biotechnol.* **2006**, *24*, 1211–1217.
2. Mulder, W. J.; Cormode, D. P.; Hak, S.; Lobatto, M. E.; Silvera, S.; Fayad, Z. A. Multimodality Nanotracers for Cardiovascular Applications. *Nat. Clin. Pract. Cardiovasc. Med.* **2008**, *5*), S103–111.
3. Jarzyna, P. A.; Gianella, A.; Skajaa, T.; Knudsen, G.; Deddens, L. H.; Cormode, D. P.; Fayad, Z. A.; Mulder, W. J. Multifunctional Imaging Nanoprobes. *Wiley Interdiscip. Rev. Nanomed. Nanobiotechnol.* **2010**, *2*, 138–150.
4. Torchilin, V. P. Multifunctional Nanocarriers. *Adv. Drug Delivery Rev.* **2006**, *58*, 1532–1555.
5. Ali, Z.; Abbasi, A. Z.; Zhang, F.; Arosio, P.; Lascialfari, A.; Casula, M. F.; Wenk, A.; Kreyling, W.; Plapper, R.; Seidel, M.; *et al.* Multifunctional Nanoparticles for Dual Imaging. *Anal. Chem.* **2011**, *83*, 2877–2882.
6. Schiffelers, R. M.; Koning, G. A.; ten Hagen, T. L.; Fens, M. H.; Schraa, A. J.; Janssen, A. P.; Kok, R. J.; Molema, G.; Storm, G. Anti-Tumor Efficacy of Tumor Vasculature-Targeted Liposomal Doxorubicin. *J. Controlled Release* **2003**, *91*, 115–122.
7. Farokhzad, O. C.; Karp, J. M.; Langer, R. Nanoparticle-Aptamer Bioconjugates for Cancer Targeting. *Expert Opin. Drug Delivery* **2006**, *3*, 311–324.
8. Pan, D.; Lanza, G. M.; Wickline, S. A.; Caruthers, S. D. Nanomedicine: Perspective and Promises with Ligand-Directed Molecular Imaging. *Eur. J. Radiol.* **2009**, *70*, 274–285.
9. Dias, A. M.; Hussain, A.; Marcos, A. S.; Roque, A. C. A Biotechnological Perspective on the Application of Iron Oxide Magnetic Colloids Modified with Polysaccharides. *Biotechnol. Adv.* **2011**, *29*, 142–155.
10. Metselaar, J. M.; Bruin, P.; de Boer, L. W.; de Vringer, T.; Snel, C.; Oussoren, C.; Wauben, M. H.; Crommelin, D. J.; Storm, G.; Hennink, W. E. A Novel Family of L-Amino Acid-Based Biodegradable Polymer-Lipid Conjugates for the Development of Long-Circulating Liposomes with Effective Drug-Targeting Capacity. *Bioconjugate Chem.* **2003**, *14*, 1156–1164.
11. Zhang, F.; Lees, E.; Amin, F.; Rivera Gil, P.; Yang, F.; Mulvaney, P.; Parak, W. J. Polymer-Coated Nanoparticles: A Universal Tool for Biolabelling Experiments. *Small* **2011**, *7*, 3113–3127.
12. Klibanov, A. L.; Maruyama, K.; Beckerleg, A. M.; Torchilin, V. P.; Huang, L. Activity of Amphipathic Poly(ethylene glycol) 5000 to Prolong the Circulation Time of Liposomes

Depends on the Liposome Size and Is Unfavorable for Immunoliposome Binding to Target. *Biochim. Biophys. Acta* **1991**, *1062*, 142–148.
13. Bhadra, D.; Bhadra, S.; Jain, P.; Jain, N. K. Pegnology: A Review of Pegylated Systems. *Pharmazie* **2002**, *57*, 5–29.
14. Ryan, S. M.; Mantovani, G.; Wang, X.; Haddleton, D. M.; Brayden, D. J. Advances in Pegylation of Important Biotech Molecules: Delivery Aspects. *Expert Opin. Drug Delivery* **2008**, *5*, 371–383.
15. Howard, M. D.; Jay, M.; Dziubla, T. D.; Lu, X. Pegylation of Nanocarrier Drug Delivery Systems: State of the Art. *J. Biomed. Nanotechnol.* **2008**, *4*, 133–148.
16. Fang, C.; Shi, B.; Pei, Y. Y.; Hong, M. H.; Wu, J.; Chen, H. Z. *In Vivo* Tumor Targeting of Tumor Necrosis Factor-Alpha-Loaded Stealth Nanoparticles: Effect of Mepeg Molecular Weight and Particle Size. *Eur. J. Pharm. Sci.* **2006**, *27*, 27–36.
17. Sheng, Y.; Yuan, Y.; Liu, C.; Tao, X.; Shan, X.; Xu, F. *In Vitro* Macrophage Uptake and *in Vivo* Biodistribution of Pla−Peg Nanoparticles Loaded with Hemoglobin as Blood Substitutes: Effect of Peg Content. *J. Mater. Sci. Mater. Med.* **2009**, *20*, 1881–1891.
18. Essa, S.; Rabanel, J. M.; Hildgen, P. Characterization of Rhodamine Loaded Peg-G-Pla Nanoparticles (NPs): Effect of Poly(ethylene glycol) Grafting Density. *Int. J. Pharm.* **2011**, *411*, 178–187.
19. Torchilin, V. P. Passive and Active Drug Targeting: Drug Delivery to Tumors as an Example. In *Handbook of Experimental Pharmacology*; Hofmann, F. B., Eds.; Springer: Berlin, 2010; pp 3−53.
20. Georgiev, G. A.; Sarker, D. K.; Al-Hanbali, O.; Georgiev, G. D.; Lalchev, Z. Effects of Poly(ethylene glycol) Chains Conformational Transition on the Properties of Mixed DMPC/DMPE-Peg Thin Liquid Films and Monolayers. *Colloids Surf. B* **2007**, *59*, 184–193.
21. Jarzyna, P. A.; Skajaa, T.; Gianella, A.; Cormode, D. P.; Samber, D. D.; Dickson, S. D.; Chen, W.; Griffioen, A. W.; Fayad, Z. A.; Mulder, W. J. Iron Oxide Core Oil-in-Water Emulsions as a Multifunctional Nanoparticle Platform for Tumor Targeting and Imaging. *Biomaterials* **2009**, *30*, 6947–6954.
22. Beer, A. J.; Schwaiger, M. Imaging of Integrin $\alpha\beta$3 Expression. *Cancer Metastasis Rev.* **2008**, *27*, 631–644.
23. Tufto, I.; Hansen, R.; Byberg, D.; Nygaard, K. H.; Tufto, J.; Davies Cde, L. The Effect of Collagenase and Hyaluronidase on Transient Perfusion in Human Osteosarcoma Xenografts Grown Orthotopically and in Dorsal Skinfold Chambers. *Anticancer Res.* **2007**, *27*, 1475–1481.
24. Hak, S.; Reitan, N. K.; Haraldseth, O.; de Lange Davies, C. Intravital Microscopy in Window Chambers: A Unique Tool to Study Tumor Angiogenesis and Delivery of Nanoparticles. *Angiogenesis* **2010**, *13*, 113–130.
25. Ashok, B.; Arleth, L.; Hjelm, R. P.; Rubinstein, I.; Onyuksel, H. *In Vitro* Characterization of Pegylated Phospholipid Micelles for Improved Drug Solubilization: Effects of Peg Chain Length and PC Incorporation. *J. Pharm. Sci.* **2004**, *93*, 2476–2487.
26. Rejman, J.; Oberle, V.; Zuhorn, I. S.; Hoekstra, D. Size-Dependent Internalization of Particles *via* the Pathways of Clathrin- and Caveolae-Mediated Endocytosis. *Biochem. J.* **2004**, *377*, 159–169.
27. Woodle, M. C.; Collins, L. R.; Sponsler, E.; Kossovsky, N.; Papahadjopoulos, D.; Martin, F. J. Sterically Stabilized Liposomes. Reduction in Electrophoretic Mobility but Not Electrostatic Surface Potential. *Biophys. J.* **1992**, *61*, 902–910.
28. Kunath, K.; Merdan, T.; Hegener, O.; Haberlein, H.; Kissel, T. Integrin Targeting Using RGD-PEI Conjugates for *in Vitro* Gene Transfer. *J. Gene. Med.* **2003**, *5*, 588–599.
29. Brooks, P. C.; Clark, R. A.; Cheresh, D. A. Requirement of Vascular Integrin $\alpha V\beta$3 for Angiogenesis. *Science* **1994**, *264*, 569–571.
30. Gennes, P. A. Polymers at an Interface: A Simplified Overview. *Adv. Colloid Interface Sci.* **1987**, *27*, 189–209.
31. Kirpotin, D.; Park, J. W.; Hong, K.; Zalipsky, S.; Li, W. L.; Carter, P.; Benz, C. C.; Papahadjopoulos, D. Sterically Stabilized Anti-Her2 Immunoliposomes: Design and Targeting to Human Breast Cancer Cells *in Vitro*. *Biochemistry* **1997**, *36*, 66–75.
32. Johnsson, M.; Edwards, K. Liposomes, Disks, and Spherical Micelles: Aggregate Structure in Mixtures of Gel Phase Phosphatidylcholines and Poly(ethylene glycol)-Phospholipids. *Biophys. J.* **2003**, *85*, 3839–3847.
33. Caswell, P.; Norman, J. Endocytic Transport of Integrins During Cell Migration and Invasion. *Trends Cell. Biol.* **2008**, *18*, 257–263.
34. Parton, R. G.; Simons, K. The Multiple Faces of Caveolae. *Nat. Rev. Mol. Cell. Biol.* **2007**, *8*, 185–194.
35. Oba, M.; Fukushima, S.; Kanayama, N.; Aoyagi, K.; Nishiyama, N.; Koyama, H.; Kataoka, K. Cyclic Rgd Peptide-Conjugated Polyplex Micelles as a Targetable Gene Delivery System Directed to Cells Possessing $\alpha\beta$3 and $\alpha\beta$5 Integrins. *Bioconjugate Chem.* **2007**, *18*, 1415–1423.
36. Oba, M.; Aoyagi, K.; Miyata, K.; Matsumoto, Y.; Itaka, K.; Nishiyama, N.; Yamasaki, Y.; Koyama, H.; Kataoka, K. Polyplex Micelles with Cyclic RGD Peptide Ligands and Disulfide Cross-Links Directing to the Enhanced Transfection *via* Controlled Intracellular Trafficking. *Mol. Pharm.* **2008**, *5*, 1080–1092.
37. Caswell, P. T.; Norman, J. C. Integrin Trafficking and the Control of Cell Migration. *Traffic* **2006**, *7*, 14–21.
38. Pelkmans, L.; Helenius, A. Endocytosis *via* Caveolae. *Traffic* **2002**, *3*, 311–320.
39. Shin, J. S.; Abraham, S. N. Caveolae as Portals of Entry for Microbes. *Microbes Infect.* **2001**, *3*, 755–761.
40. Gianella, A.; Jarzyna, P. A.; Mani, V.; Ramachandran, S.; Calcagno, C.; Tang, J.; Kann, B.; Dijk, W. J.; Thijssen, V. L.; Griffioen, A. W.; *et al*. Multifunctional Nanoemulsion Platform for Imaging Guided Therapy Evaluated in Experimental Cancer. *ACS Nano* **2011**, *5*, 4422–4433.
41. Mulder, W. J.; Strijkers, G. J.; Habets, J. W.; Bleeker, E. J.; van der Schaft, D. W.; Storm, G.; Koning, G. A.; Griffioen, A. W.; Nicolay, K. MR Molecular Imaging and Fluorescence Microscopy for Identification of Activated Tumor Endothelium Using a Bimodal Lipidic Nanoparticle. *FASEB J.* **2005**, *19*, 2008–2010.
42. Cai, W.; Chen, K.; Li, Z. B.; Gambhir, S. S.; Chen, X. Dual-Function Probe for PET and Near-Infrared Fluorescence Imaging of Tumor Vasculature. *J. Nucl. Med.* **2007**, *48*, 1862–1870.
43. Oostendorp, M.; Douma, K.; Hackeng, T. M.; van Zandvoort, M. A.; Post, M. J.; Backes, W. H. Pharmacokinetics of Contrast Agents Targeted to the Tumor Vasculature in Molecular Magnetic Resonance Imaging. *Contrast Media Mol. Imaging* **2010**, *5*, 9–17.
44. Kessinger, C. W.; Togao, O.; Khemtong, C.; Huang, G.; Takahashi, M.; Gao, J. Investigation of *in Vivo* Targeting Kinetics of α*(V)Beta*β(3)-Specific Superparamagnetic Nanoprobes by Time-Resolved MRI. *Theranostics* **2011**, *1*, 263–273.
45. Erikson, A.; Tufto, I.; Bjonnum, A. B.; Bruland, O. S.; Davies Cde, L. The Impact of Enzymatic Degradation on the Uptake of Differently Sized Therapeutic Molecules. *Anticancer Res.* **2008**, *28*, 3557–3566.